Materials Today Communications 50 (2026) 114222

Contents lists available at ScienceDirect

Materials Today Communications

journal homepage: www.elsevier.com/locate/mtcomm

Influence of isothermal post-treatment on tribocorrosion behaviour of laser powder bed fusion-processed β-type Ti-Nb alloy

Adnan Akman [a,b,*], Yohan Douest [c,d], Jaqueline Gehlmann [e], Avinash Hariharan [f], Christian Haase [g,h], Ana-Maria Trunfio Sfarghiu [i], Nicolas Courtois [c], Benoit Ter-Ovanessian [d], Stefan Pilz [a], Martina Zimmermann [b], Annett Gebert [a]

[a] Leibniz Institute for Solid State and Materials Research Dresden, Helmholtzstr. 20, Dresden 01069, Germany
[b] Institute of Materials Science, TU Dresden, Helmholtzstr. 7Dresden 01069, Germany
[c] Anthogyr SAS, Sallanches F-74700, France
[d] Univ. Lyon, INSA de Lyon, MATEIS, UMR CNRS 5510, Villeurbanne 69621, France
[e] Central Facility for Electron Microscopy, RWTH Aachen University, Aachen 52074, Germany
[f] Steel Institute, RWTH Aachen University, Aachen 52072, Germany
[g] Chair Materials for Additive Manufacturing, TU Berlin, Berlin 10587, Germany
[h] Center for 3D Technologies, TU Berlin, Berlin 10623, Germany
[i] Univ. Lyon, INSA de Lyon, LaMCoS, UMR CNRS 5259, Villeurbanne 69621, France

ARTICLE INFO

Keywords:
Titanium alloy
Tribocorrosion
Laser powder bed fusion
Biomaterial

ABSTRACT

Ti-Nb alloys are well-regarded implant materials thanks to their high corrosion resistance and good biocompatibility. Nonetheless, their cast and solution-treated forms suffer from limited mechanical strength. LPBF-processed Ti-Nb alloys hold significant potential for customized implants. Applying post-heat treatments, particularly isothermal age-hardening, can strengthen these alloys and improve their resistance to the biomechanical loads encountered in service. However, load-bearing implants are prone to tribocorrosion due to the relative motion between implant components or between the implant and surrounding tissue in body fluids.

This study investigates the mechanical, corrosion, and tribocorrosion properties of post-treated LPBF-produced β-type Ti-42Nb alloys, and compares their performance with both as-built LPBF Ti-42Nb and conventional Ti-6Al-4V ELI. Results show that isothermal heat treatment is effective in increasing the mechanical properties by introducing ω_{iso} precipitates for Ti-42Nb (LPBF-300 °C 30 h) and α_{iso}'' precipitates for Ti-42Nb (LPBF-450 °C 30 h) to the single β-phase microstructure. Tribocorrosion behaviour was investigated under open circuit potential (OCP) and anodic potentiostatic polarization conditions (0.6 V vs. Ag|AgCl) in phosphate-buffered saline (PBS) using a reciprocating pin-on-disk tribometer. The formation of precipitates does not adversely affect the passive film, indicating that its stability is maintained by the strong passivating nature of Ti-Nb alloys. However, the tribocorrosion resistance declines following isothermal heat treatment, likely due to the rapid detachment of hard and brittle precipitates, leading to increased material loss. Nevertheless, controlling the distribution of precipitates in LPBF-fabricated Ti-42Nb alloys may enhance their performance for implant use.

1. Introduction

Titanium alloys are ideal for load-bearing implants due to their strength, corrosion resistance, and biocompatibility. However, commonly used materials like cp-Ti and Ti-6Al-4V raise clinical concerns, as their Young's modulus (100–120 GPa) is much higher than that of cortical bone (4–30 GPa) [1,2]. This disparity creates a mismatch between the implant and the surrounding bone, leading to aseptic implant loosening caused by bone resorption, a phenomenon known as stress shielding [3].

* Corresponding author at: Leibniz Institute for Solid State and Materials Research Dresden, Helmholtzstr. 20, Dresden 01069, Germany.
E-mail addresses: a.akman@ifw-dresden.de (A. Akman), yohan.douest@gmail.com (Y. Douest), gehlmann@gfe.rwth-aachen.de (J. Gehlmann), avinash.hariharan@iehk.rwth-aachen.de (A. Hariharan), christian.haase@tu-berlin.de (C. Haase), ana-maria.sfarghiu@insa-lyon.fr (A.-M.T. Sfarghiu), nicolas.courtois@anthogyr.com (N. Courtois), benoit.ter-ovanessian@insa-lyon.fr (B. Ter-Ovanessian), pilzstefan@outlook.com (S. Pilz), martina.zimmermann@tu-dresden.de (M. Zimmermann), a.gebert@ifw-dresden.de (A. Gebert).

https://doi.org/10.1016/j.mtcomm.2025.114222
Received 1 September 2025; Received in revised form 17 October 2025; Accepted 30 October 2025
Available online 31 October 2025

Recently, β-type Ti alloys have attracted interest as they primarily consist of non-toxic elements such as niobium (Nb), zirconium (Zr), molybdenum (Mo), and tantalum (Ta) [4]. These alloys offer excellent mechanical compatibility along with suitable strength for implant applications. Among them, Ti-Nb-based alloys have gained significant attention [5–9]. β-type Ti-Nb alloys, in their cast and solution-treated states, exhibit a low Young's modulus between 55 and 65 GPa, providing an opportunity to minimize the stress-shielding effect [1]. Additionally, their outstanding corrosion resistance and biocompatibility make Ti-Nb alloys highly promising candidates for use in implants [10–12].

However, β-type Ti-Nb alloys exhibit moderate yield strength (ranging from 300 to 500 MPa) in their cast and solution-treated states under loading, which is comparatively lower than that of commercial Ti-6Al-4V [13,14]. Various strengthening strategies have been widely explored to improve the strength of Ti-Nb-based alloys while maintaining a low Young's modulus. These methods include work hardening, grain refinement, and isothermal age hardening [15,16]. Research has demonstrated that work hardening significantly increases the static strength of Ti-Nb alloys, achieving values up to 900 MPa. However, under dynamic loading conditions, it proves insufficient to notably enhance mechanical properties when compared to isothermally aged alloys [17,18]. In contrast, grain refinement serves as a reliable strategy for mechanical strengthening, although its effect is primarily limited to increasing strength without notably affecting Young's modulus [14,15].

Among the various strengthening techniques, the introduction of alpha (α) and omega (ω) phases into the microstructure of Ti-Nb alloys through isothermal aging has emerged as a promising method for achieving the desired strength under both static and dynamic loads [18–22]. However, since the α and ω phases inherently possess a higher Young's modulus than the β phase ($E_{\omega} > E_{\alpha'} > E_{\alpha''} > E_{\beta}$) [23], their presence can gradually increase the Young's modulus of Ti-Nb alloys as the isothermal heat treatment duration extends. Moreover, the physical and mechanical properties of these alloys are significantly influenced by the size, morphology, and volume fraction of the precipitates. Therefore, gaining a comprehensive understanding of the formation kinetics, growth behaviour, and mechanical response of these precipitates is crucial for optimizing their performance [24,25].

Recently, additive manufacturing techniques, such as laser powder bed fusion (LPBF), have gained significant attention for their exceptional flexibility in producing orthopedic load-bearing implants [26,27]. These methods allow for the fabrication of complex geometries and the development of patient-specific implants, whether in bulk or lattice-based designs [28–33].

LPBF-produced β-type Ti-Nb alloys exhibit superior mechanical properties compared to those manufactured using conventional methods [25,34]. Additionally, LPBF enables precise control over the local mechanical properties of components by adjusting various processing parameters, such as laser speed and power. This capability allows for the customization of implants to match the mechanical loads experienced by human bone [35,36]. However, components manufactured through LPBF often experience mechanical anisotropy and the accumulation of residual stresses. Therefore, post-heat-treatment techniques are essential for refining the microstructural and mechanical properties [37].

Until now, limited research has been conducted regarding the post-heat treatment of LPBF-produced Ti-Nb alloys. Hein et al. [38] studied aging treatment at 500 °C for LPBF-processed Ti-24 Nb-4Zr-8Sn. The results showed that as-built samples have yield strengths of 340–490 MPa, tensile strength around 706 MPa, elongation of about 20 %, and a Young's modulus of 50 GPa. In contrast, post-treated samples exhibit increased yield strength of 812 MPa, tensile strength between 871 and 931 MPa, lower elongation of around 12 %, and a higher Young's modulus of 75 GPa. However, it is essential to address crack initiation and propagation along grain boundary precipitates, as they contribute to premature and brittle fracture [25].

On the other hand, the effect of isothermal ω precipitates on the deformation behaviour of conventionally produced Ti-40Nb alloy was investigated [24]. The results revealed that the presence of ω_{iso} precipitates hinders stress-induced transformation (SIM) and deformation twinning during plastic deformation, thereby limiting long-range martensitic transformations. The mechanical behaviour of the age-hardened Ti-40Nb alloy was found to be dependent on the volume fraction of ω_{iso} precipitates, which can be controlled with the temperature and duration of the age-hardening process. The yield strength of the alloy ranged from 410 to 900 MPa, and Young's modulus varied between 70 and 95. The higher Young's modulus values of 95 GPa are attributed to the ω_{iso} phase's volume fraction and its inherently high modulus. The presence of the ω_{iso} phase not only inhibits the transformation to α_{SIM}'' (stress-induced martensite) but, in certain forms, can also lead to embrittlement, compromising the structural integrity of the alloy [19,39]. Therefore, it is essential to establish a carefully designed post-heat treatment process by precisely controlling time and temperature to achieve the desired mechanical properties for implant applications.

Although isothermal aging treatment can achieve the desired mechanical properties, metallic implants remain vulnerable to degradation caused by tribocorrosion, which is a combined effect of mechanical wear and electrochemical corrosion in physiological environments. In addition, under tribocorrosion conditions, the simultaneous influence of wear and corrosion may cause excess ion release and severe deterioration [40–42]. Therefore, it is critical to investigate the synergistic interaction between corrosion and wear in physiological environments to develop improved implant materials [43].

In our previous work [44], the corrosion and tribocorrosion behaviour of LPBF-produced β-type Ti-42Nb alloy, fabricated using both Gaussian and high-power top hat laser configurations, was analyzed alongside conventionally manufactured β-type Ti-45Nb and α+ β-type Ti-6Al-4V ELI alloys. The results indicate that the passivation behaviour of LPBF-produced alloys plays a more critical role in corrosion resistance than their microstructural characteristics. Additionally, LPBF-manufactured alloys demonstrate superior tribo-electrochemical performance compared to conventionally produced Ti-45Nb. The variations in volume loss are primarily linked to the microhardness of the alloys, with mechanical wear being the dominant factor influencing volume loss.

This study investigated the effect of post-heat treatments on LPBF-fabricated Ti-42Nb specimens, focusing on their resulting microstructure, mechanical behaviour (tensile testing), and corrosion and tribocorrosion performance. The as-built, single-phase β-type samples, produced using a Gaussian laser configuration, underwent post-heat treatments at 300 °C and 450 °C for 30 h. These heat treatment conditions were established based on the stable α-β and metastable ω-β phase diagrams [22] as well as previous experimental studies on Ti-Nb alloys [24]. Analysis revealed the formation of ω_{iso} precipitates in the Ti-42Nb (LPBF-300 °C 30 h) sample, and the α_{iso}'' precipitates were observed in the Ti-42Nb (LPBF-450 °C 30 h) specimen. Their properties were evaluated in comparison to both the as-built Ti-42Nb samples and conventionally manufactured Ti-6Al-4V ELI. This comparison highlighted how microstructural features affect the tribo-electrochemical response, revealing the fundamental degradation mechanisms under various tribocorrosion conditions and offering guidance for designing advanced hard-tissue implants. Overall, by demonstrating the role of controlled precipitate formation in performance and connecting microstructural engineering to multi-property behaviour, this study delivers novel insights and practical strategies for optimizing LPBF-fabricated Ti-42Nb alloys for biomedical applications.

2. Experimental methods

2.1. Preparation of the alloy and post-treatment

Pre-alloyed, gas-atomized Ti-42Nb (wt%) powder with a particle size

range of 10–63 μm was provided by TANIOBIS GmbH. The LPBF process was carried out using an SLM 280 Generation 2.0 machine (SLM Solutions Group AG, Germany). The samples were processed with a Gaussian laser. LPBF processing of 26 mm x 16 mm x 7 mm cuboids was conducted with an SLM280 Generation 2.0 dual laser machine (SLM Solutions Group AG, Germany). The process parameters included a scanning speed of 1000 mm/s, a laser power of 250 W, and a layer thickness of 50 μm. A stripe pattern with a hatch distance of 100 μm and a vector rotation of 67° was applied. [25]. After the LPBF process, cylindrical alloy samples were cut perpendicular to the building direction (BD) with a diameter of 7 mm and a thickness of 3 mm by electrical discharge machining (EDM).

The alloy samples were subjected to post-heat treatments at 300 °C and 450 °C for 30 h to promote precipitate formation and enhance the alloy's strength. The samples were enclosed in fused silica tubes under a protective Ar atmosphere to mitigate the uptake of interstitial elements. After the heat treatments, cooling was carried out through water quenching.

2.2. Microstructure characterization

The specimens designated for microstructural examinations underwent grinding using SiC paper ranging from grit 400–2500. A polishing step was performed by utilizing a mixture composed of colloidal SiO_2 (90 vol%) and H_2O_2 (10 vol%). Scanning electron microscope (SEM) imaging was conducted using a Leo Gemini 1530 (Zeiss AG, Germany). Transmission electron microscopy (TEM) was performed to reveal the presence of the precipitates. The TEM lamellae were prepared using the dual beam focused ion beam (FIB) with standard liftout and preparation procedures [45]. A Tecnai F20 TEM from FEI, operating at an accelerating voltage of 200 kV, was used for the characterization of the FIB lamellae. The TEM device is equipped with a side-entry Veleta camera (S04 F, EMSIS), which offers a resolution of 4 megapixels. The Veleta camera was used for image acquisition and recording the selected area diffraction patterns. The reference data for identification of the crystal structures are from the online ICSD database with CollCode645545 for the β phase, CollCode150817 for the ω phase and CollCode105248 for the α'' phase. In addition, synchrotron X-ray diffraction (SXRD) experiments were conducted at PETRA III (Deutsches Elektronen-Synchrotron, Hamburg, Germany). For both as-built and heat-treated samples, two-dimensional X-ray diffraction patterns were obtained at the High Energy Materials Science (HEMS) beamline using an X-ray beam with an energy of 102.69 keV. More details about the SXRD procedure can be found elsewhere [25].

2.3. Mechanical testing

To examine the effects of heat treatments on mechanical properties, flat bar tensile samples were machined from heat-treated cuboids. These samples had a gauge length of 5.5 mm, a width of 1 mm, and a thickness of 0.85 mm, and they were extracted perpendicular to the building direction (BD). Mechanical testing was performed using uniaxial tensile tests with a tensile-compression module from Kammrath & Weiss GmbH (Germany), featuring a 5 kN load cell and an extension rate of 0.0175 mm/s. At least three samples were tested for each condition to ensure reproducibility.

Vickers microhardness ($HV_{0.1}$) was measured with a Falcon 600 indenter on polished samples by applying a 1 N load. The average hardness values with standard deviations are the result of 10 consecutive measurements.

2.4. Corrosion testing

Electrochemical tests were conducted in a phosphate-buffered saline (PBS) solution at room temperature to evaluate the corrosion performance of LPBF-processed post-treated β-type Ti-42Nb alloys, together with the as-built state and conventional Ti-6Al-4V ELI. Before testing, the alloy samples were mechanically ground using SiC emery paper, progressing from grit 320–1200.

The corrosion test was performed using a Solartron XM ModuLab potentiostat coupled with a three-electrode cell setup. Titanium alloys served as the working electrode (WE), while a platinum wire was employed as the counter electrode (CE) with a geometrical surface area of 0.38 cm^2. The potentials were measured versus the silver chloride electrode (Ag|AgCl, E(Ag|AgCl) = 0.197 V vs. SHE) as the reference electrode (RE). The corrosion behaviour of the alloys under investigation was evaluated by measuring the open circuit potential (OCP) for 30 min to stabilize the system. Then, potentiodynamic polarization measurement was conducted across a potential range from −0.3 V (vs. OCP) to 1 V (vs. Ag|AgCl) at a scan rate of 0.5 mV/s. Tafel extrapolation was performed using ECLab software (v11.36). All corrosion experiments were repeated three times to ensure reproducibility.

2.5. Tribocorrosion testing

Tribocorrosion tests were conducted at room temperature in phosphate-buffered saline (PBS) using a pin-on-disk tribometer at room temperature. A Gamry potentiostat (model Ref-600) was employed in a three-electrode setup to monitor the electrochemical response of the alloys under mechanical loading. The studied alloys served as the working electrode (WE), paired with an alumina ball (6 mm in diameter) as the counter body. A platinum wire was used as the counter electrode (CE), while a silver chloride electrode (Ag|AgCl) acted as the reference electrode (RE). The tests were carried out under a reciprocating sliding frequency of 0.5 Hz with an applied load of 4 N (with a sliding displacement of around 2 mm). For tribocorrosion testing, the sample plane perpendicular to the building direction (BD) was investigated for LPBF-produced alloys. Before testing, the alloy samples were mechanically ground using SiC emery papers, progressing from grit 320–1200. A consistent sample preparation procedure was applied to all specimens to ensure uniform surface conditions across the different heat treatment groups. This approach aimed to minimize variations in surface roughness and their potential influence on tribocorrosion.

Two tribocorrosion test approaches were employed: (i) sliding under open circuit potential (OCP) conditions and (ii) sliding under a fixed anodic potential of 0.6 V vs. Ag|AgCl. Sliding under OCP represents *a* realistic scenario in which the potential evolves naturally due to the environment and tribological interactions, whereas the anodic potentiostatic approach allows investigation of the depassivation and repassivation kinetics of the passive film. All experiments were repeated twice to ensure reproducibility.

i) Open circuit potential (OCP) measurements: The OCP was recorded for 30 min to reach a steady state, followed by 30 min of sliding while maintaining the OCP to evaluate tribocorrosion behaviour. After stopping the sliding, the OCP was monitored for an additional 30 min.
ii) Anodic potentiostatic polarization measurements: The alloys were subjected to potentiostatic polarization at 0.6 V vs. Ag|AgCl for 30 min until a steady-state current was achieved. Sliding was then performed for 30 min under the same polarization, after which the motion ceased, and the anodic current was monitored for another 30 min.

2.6. Characterization of wear tracks

The wear morphologies were examined using scanning electron microscopy (SEM) and 3D confocal profilometry. A Zeiss Leo Gemini 1530 SEM was utilized to capture detailed images of the worn features of the studied alloy samples. The total volume loss (V_{tot}) and wear depth (D) of the worn areas were evaluated with a non-contact S Neox 3D confocal profilometer. The areas of interest were investigated with the

Sensomap standard (v. 6.7) software.

3. Results

3.1. Microstructural characterization

Ti-42Nb alloy samples were successfully fabricated using the laser powder bed fusion (LPBF) process with a Gaussian laser, achieving a high relative density of 99.96 %. The rapid solidification and cooling rates inherent to LPBF resulted in a single β-type microstructure without any additional phases [25,34]. The use of a Gaussian laser in LPBF creates a hemispherical melt pool with strong thermal gradients, resulting in irregular, randomly oriented grains and very weak texture, producing an almost isotropic microstructure [34]. The Ti-42Nb alloy samples underwent post-heat treatments at two different temperatures (300 °C for 30 h and 450 °C for 30 h). The solidification structure of post-treated alloys exhibited a characteristic cellular/cellular-dendritic pattern typical of LPBF-processed Ti-42Nb alloys (not shown here), as discussed before [25,34]. The X-ray diffraction (SXRD) analysis and TEM images for post-treated LPBF-produced Ti-42Nb alloy are illustrated in Fig. 1 together with diffraction patterns for the areas shown in the TEM images.

SXRD data (Fig. 1a) indicate that after 30 h of isothermal aging at 300 °C, the ω_{iso} phase appeared alongside the β phase, with no evidence of additional phases. A TEM image (Fig. 1b) of the LPBF-produced Ti-42Nb sample aged for 30 h reveals densely and uniformly distributed nanosized ω_{iso} precipitates (bright phase) within the matrix. The findings fit well with the previous literature for isothermal aging of conventionally produced Ti-40Nb alloys [24].

After 30 h of isothermal treatment at 450 °C, the crystal structure of the secondary phase has been identified as orthorhombic α_{iso}'' according to SXRD data (Fig. 1c). This thermally activated α_{iso}'' formation serves as an intermediate step toward the stable α phase. As reported in previous work on LPBF-produced Ti-42Nb alloys [25], isothermal aging at 450 °C leads the supersaturated β phase to first form a metastable orthorhombic α_{iso}'' phase. This phase initially precipitates at grain boundaries as ~50 nm particles after 4 h and grows to ~25 % volume fraction by 30 h. With prolonged aging, the precipitates coarsen and progressively transform toward the stable α phase. The overall process follows a diffusion-controlled pathway, governed by grain-boundary nucleation and Nb diffusion. Similar observations were made before for Ti-based alloys [25,46,47]. A TEM image (Fig. 1d) of the LPBF-produced Ti-42Nb sample aged for 30 h reveals nanosized α_{iso}'' precipitates within the matrix. The morphology and arrangement of these precipitates closely resemble those observed in previous studies [48,49].

3.2. Mechanical properties

To evaluate the effect of isothermal aging treatment on the mechanical properties of LPBF-produced Ti-42Nb alloys, tensile test samples with the loading direction perpendicular to the building direction (BD) were prepared. The tensile test curves for the samples in the as-built state and after post-treatments are illustrated in Fig. 2.

The mechanical properties are derived from the stress-strain curves. In its as-built state, the alloy exhibits yield strength and ultimate tensile strength, with values of 700 ± 1 MPa and 715 ± 1 MPa, respectively. At the same time, this condition demonstrates elongation at fracture around 20.1 ± 0.7 % and a low Young's modulus of 65 ± 1 GPa, which outperforms cast and solution-treated β-type Ti-Nb alloys in terms of mechanical properties [5,14,50,51]. In addition, compared to other additively manufactured states of the same alloy, the obtained values fall within a similar range [34].

For the LPBF-produced alloy heat-treated at 300 °C for 30 h, a significant increase in strength was observed. Yield strength values reached 850 ± 2 MPa, while tensile strength reached 835 ± 4 MPa; a noticeable decline in tensile stress after yielding was observed. In addition, this enhancement is accompanied by a significant amount of total elongation (17.9 ± 2.2 %). Additionally, Young's modulus of 94 ± 5 GPa after 30 h was observed, which is associated with the high intrinsic Young's modulus of the ω_{iso} phase. Similar findings in terms of mechanical properties were observed for the age-hardened (300 °C for 30 h) Ti-40Nb alloy. The precipitates result in a uniform distribution throughout the microstructure with a sluggish characteristic due to the decreased solute diffusion of Nb in Ti as the Nb content increases [24].

According to the literature, ω_{iso} precipitates enhance hardening and influence deformation mechanisms (twinning, phase transformation,

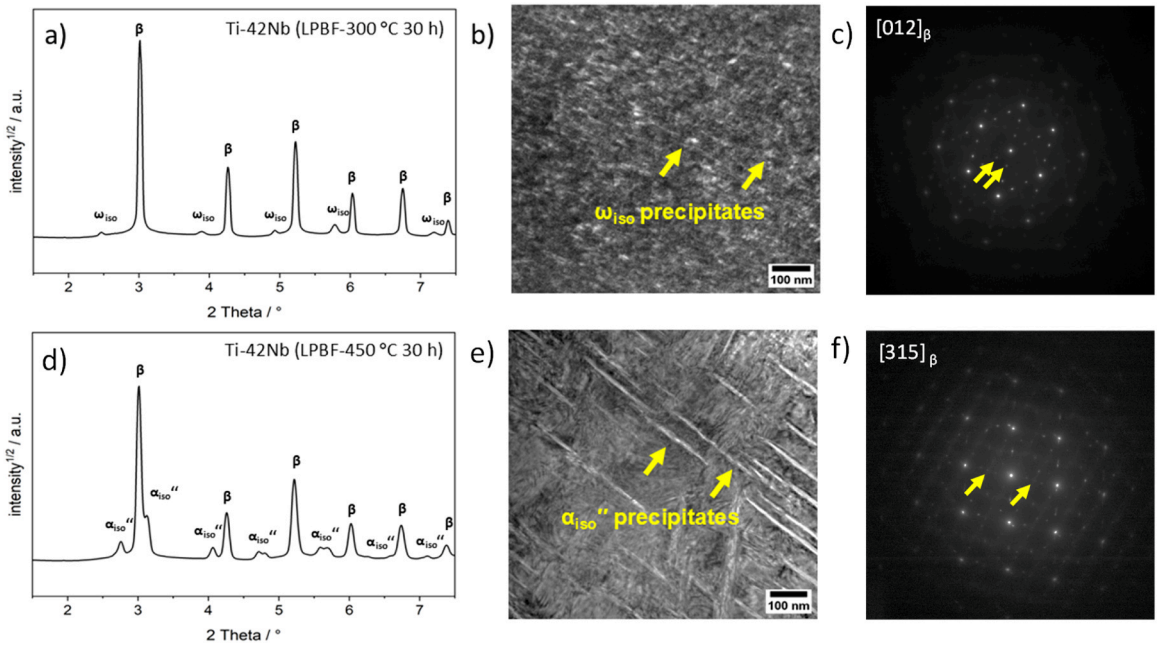

Fig. 1. X-ray diffraction (SXRD) analysis and corresponding TEM images for heat-treated LPBF-produced Ti-42Nb alloys. Images a) and b) belong to the Ti-42Nb (LPBF-300 °C 30 h), and d) and e) belong to the Ti-42Nb (LPBF-450 °C 30 h) alloy states. Additionally, the diffraction patterns for c) Ti-42Nb (LPBF-300 °C 30 h) and f) Ti-42Nb (LPBF-450 °C 30 h) alloy states are represented.

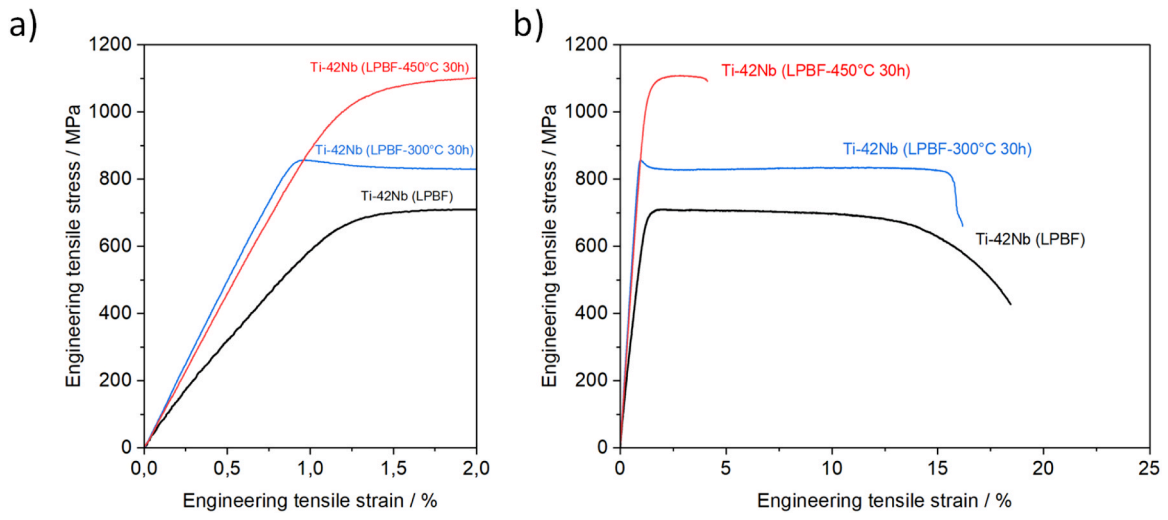

Fig. 2. Engineering stress-strain curves of LPBF-produced Ti-42Nb alloy in the as-built state (LPBF), together with post-treated Ti-42Nb samples (LPBF-300 °C 30 h) and (LPBF-450 °C 30 h). a) Magnified view of the linear region and b) complete stress-strain curve.

and dislocation slip) in β-type Ti-based alloys, depending on composition and processing history. Kim et al. [52] demonstrated that ω-precipitates increase stress for slip deformation while suppressing α''-phase formation as their volume fraction grows. This effect is attributed to Nb depletion in the ω-phase, leading to Nb enrichment in the β-matrix, which lowers the martensitic transformation temperature and stabilizes the β-phase. According to the investigations on β-type metastable Ti alloys [53], plastic deformation was localized in ω-depleted dislocation channels. These channels consisted of a high amount of dislocations moving in these channels towards the free surface of the material, probably using multiple slip systems rather than single planar slip. Thus, this could be an explanation for the high amount of uniform elongation for the LPBF-produced alloy treated at 300 °C for 30 h.

LPBF-produced alloy treated at 450 °C for 30 h showed a significant increase in strength. Yield strength values reached 1059 ± 17 MPa, while tensile strength reached 1124 ± 13 MPa. However, this enhancement is accompanied by a reduction in total elongation (4.1 ± 0.5 %). Additionally, Young's modulus of 87 ± 1 GPa after 30 h was obtained due to the presence of α_{iso}'' precipitates with high intrinsic Young's modulus.

The morphology, size, and distribution of precipitates are greatly influenced by the local chemical composition and phase transformation kinetics. In both cases, after the post-heat treatment, precipitates result in a uniform distribution throughout the microstructure. For both cases, isothermal heat-treated alloys exhibit a still lower Young's modulus and higher tensile strength values than conventional Ti-6Al-4V [1]. However, further research is necessary to achieve a balanced combination of a low Young's modulus and increased strength.

Vickers microhardness ($HV_{0.1}$) values are 226 ± 6 $HV_{0.1}$ *and* 348 ± 5 $HV_{0.1}$ for LPPF-produced as-built Ti-42Nb alloy and conventional Ti-6Al-4V ELI, respectively. For the age-hardened alloy samples, hardness values are 302 ± 19 $HV_{0.1}$ (Ti-42Nb (LPBF-300 °C 30 h)) and 335 ± 3 $HV_{0.1}$ (Ti-42Nb (LPBF-450 °C 30 h)). These increases in hardness relative to the as-built condition are directly linked to the formation of precipitates within the microstructure during the post-heat treatment process. Such precipitates act as barriers to dislocation motion, thereby enhancing the alloy's resistance to plastic deformation. Overall, although the heat-treated Ti-42Nb alloys reach hardness levels comparable to those of the Ti-6Al-4V ELI alloy, adjusting the heat treatment parameters, such as temperature and duration, provides a way to optimize hardness alongside other key mechanical properties. This underscores the crucial role of post-processing heat treatments in fine-tuning the performance of LPBF-produced Ti-Nb alloys, particularly for biomedical applications.

3.3. Corrosion tests

Electrochemical tests were performed to investigate the corrosion behaviour of the studied alloys. Initially, OCP was measured in PBS solution for 30 min to reach a steady state. Then, potentiodynamic polarization experiments were conducted, as shown in Fig. 3. All tested alloys exhibit similar polarization behaviour with an initial low current density value (in the range of a few μA/cm^2) at the corrosion potential (E_{corr}). E_{corr} of the studied alloys is in the range of −0.258 ÷ −0.160 V vs. Ag|AgCl, and the corrosion current densities (i_{corr}) are in the range of 0.22 ÷ 0.53 μA/cm^2. The anodic region of the potentiodynamic polarization curves shows a stable passive region during the anodic scan till 1 V vs. Ag|AgCl due to the formation of the protective and stable passive film, which is commonly observed in valve metals (Ti and Nb) [10,11]. The calculated passivation densities (i_{pass} at 0.6 V (vs. Ag|AgCl)) are in the range of 5.2 ÷ 8.5 μA/cm^2. The overall polarization response of the LPBF-produced β-type Ti-42Nb alloys is similar. Among post-heat-treated alloys, no significant difference was found, and corrosion and passivation current densities are similar to conventionally produced Ti-6Al-4V ELI. The presence of ω_{iso} nanoprecipitates for

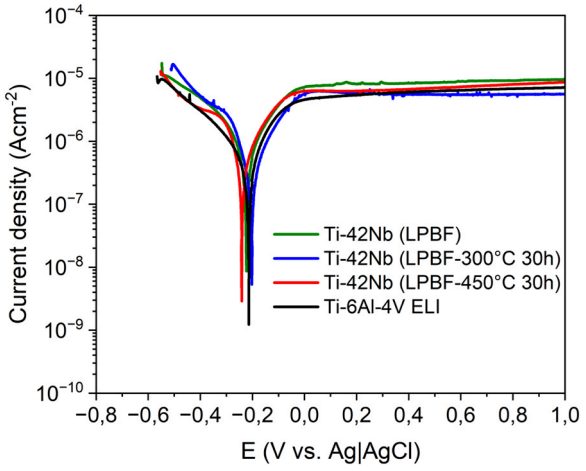

Fig. 3. Potentiodynamic polarization curves of Ti-42Nb (LPBF), Ti-42Nb (LPBF-300 °C 30 h), Ti-42Nb (LPBF-450 °C 30 h), and Ti-6Al-4V ELI alloy states in PBS solution after 30 min OCP stabilization.

Ti-42Nb (LPBF-300 °C 30 h) and the presence of α_{iso}'' nanoprecipitates for Ti-42Nb (LPBF-450 °C 30 h) do not yield a negative response in the passive film behaviour, indicating that its stability is preserved.

3.4. Tribocorrosion test under open circuit potential conditions

The open circuit potential (OCP) was assessed before, during, and after reciprocating sliding and the potential change over time for the studied alloy samples is illustrated in Fig. 4.

Before sliding, all alloys show stable potential values due to the presence of a passive film on the surface under OCP conditions. However, a sudden drop in potential was observed at the start of sliding (at 1800 s), indicating partial or complete destruction of the passive film (depassivation) at the contact region between the pin and the alloy surfaces. The fluctuations during sliding (1800 s to 3600 s) result from the repetitive formation and removal of the passive film under OCP conditions. In addition, line current fluctuation caused by the rapid movement of the pin (due to its relatively high frequency) alters the exchange processes between the cathodic and anodic sites on the surface. The OCP during sliding reflects the mixed potential of both worn and unworn areas and is influenced by the ratio of these areas. The oxide film in the contact area undergoes mechanical damage during sliding, activating the wear track and causing a significant drop in potential. This exposure reveals fresh bare metal to the corrosive environment, leading to the formation of a new oxide film. The OCP stabilizes once the formation and removal rates of the oxide film reach equilibrium [54].

After sliding (from 3600 s), all studied alloy states display a positive trend in potential, approaching the values recorded before sliding, due to the repassivation of the worn areas. The potentials before (E_{OCP}^{start}), during ($E_{OCP}^{sliding}$), and after (E_{OCP}^{end}) sliding were recorded. In addition, the potential drop ($|\Delta E|$) during the initial seconds of the sliding was recorded, as illustrated in Fig. 5. The lowest potential drop belongs to Ti-6Al-4V ELI, which represents the ability of the alloy to uphold a steady state equilibrium between depassivation and repassivation states during reciprocating sliding under OCP conditions. However, for the LPBF-produced alloys (as-built and isothermal-heat-treated), no significant difference was found between recorded potentials before, during, and after sliding.

3.5. Tribocorrosion test under applied anodic potential conditions

Tribocorrosion experiments were conducted under anodic potentiostatic polarization (at 0.6 V vs. Ag|AgCl) conditions to investigate the repassivation and depassivation kinetics of the studied alloys. The applied potential was selected from the passive region of the potentiodynamic polarization curves (Fig. 3). The anodic potentiostatic current values were monitored before, during, and after reciprocating sliding. The change in anodic current under the applied potential over time for the studied alloy samples is shown in Fig. 6, together with the recorded average currents before, during, and after reciprocating sliding, summarized in Table 1.

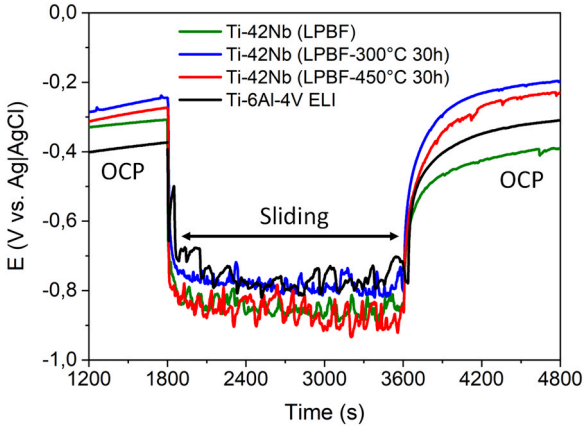

Fig. 4. Open circuit potential (OCP) evolution of Ti-42Nb (LPBF), Ti-42Nb (LPBF-300 °C 30 h), Ti-42Nb (LPBF-450 °C 30 h), and Ti-6Al-4V ELI alloy states in PBS solution. The arrow indicates the reciprocating sliding occurring between 1800 s and 3600 s.

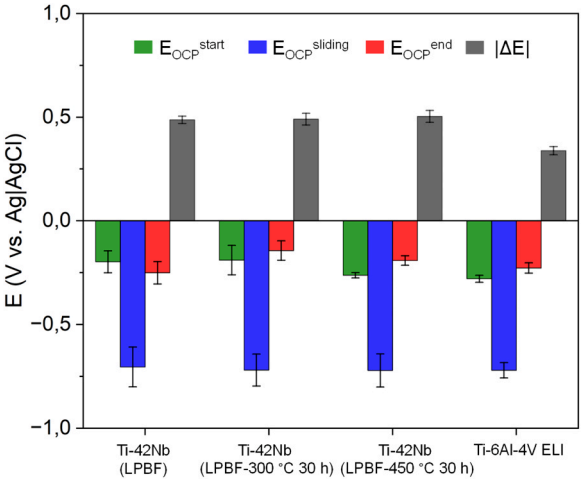

Fig. 5. Representation of the electrochemical parameters obtained from the tribocorrosion curves for OCP conditions, potentials before (E_{OCP}^{start}), during ($E_{OCP}^{sliding}$), and after (E_{OCP}^{end}) sliding were recorded together with the potential drop ($|\Delta E|$) during the initial seconds of the sliding for Ti-42Nb (LPBF), Ti-42Nb (LPBF-300 °C 30 h), Ti-42Nb (LPBF-450 °C 30 h), and Ti-6Al-4V ELI alloy states. Potential values are reported vs. Ag/AgCl (E(Ag|AgCl) = 0.197 V vs. SHE). Error bars were calculated based on the standard deviations obtained from two independent tribocorrosion experiments.

Before sliding begins (till 1800 s), the current remains stable for all studied alloy samples, and the measured anodic current indicates the presence of a passive film on the alloy surfaces, formed under applied potential. Upon the initiation of sliding (from 1800 s), all alloys show a sudden increase in recorded currents under anodic potential during the first few seconds due to the mechanical destruction of the passive films caused by the pin. The fluctuation in current during sliding (1800 s to 3600 s) is evident due to the continuous removal (depassivation) and reformation (repassivation) of the passive film. As the oxide film in the contact area experiences mechanical damage during sliding, the wear track becomes activated, leading to a notable rise in current. The current eventually stabilizes when the formation and removal of the oxide film reach equilibrium [55]. The intensity of the fluctuations in current during sliding for the LPBF-produced alloys is similar to each other and greater than those observed in Ti-6Al-4V ELI, as illustrated in Fig. 6. For the LPBF-produced alloy in the as-built state, the current behaviour (Fig. 6a) could be attributed to the accumulation of wear debris on the surface after sliding for 2400 s or late stabilization between the depassivation and repassivation states. After sliding, the recorded currents stabilize due to the reformation of passive films on the worn areas. The recorded current values during passive film growth and after sliding (0.6 V vs. Ag|AgCl) for post-heat-treated alloys are slightly higher than those for LPBF-produced Ti-42Nb in the as-built state and Ti-6Al-4V ELI, as shown in Table 1. This difference may be due to the defective nature of the passive films formed under the applied anodic potential. In addition, similar current values during sliding under anodic polarization conditions for the LPBF-produced alloys can be attributed to their similar passive film characteristics (Ti-Nb-based oxide formation).

3.6. Analysis of worn surfaces

The worn areas were examined with SEM to study their surface features and to reveal the wear mechanisms. SEM images of worn

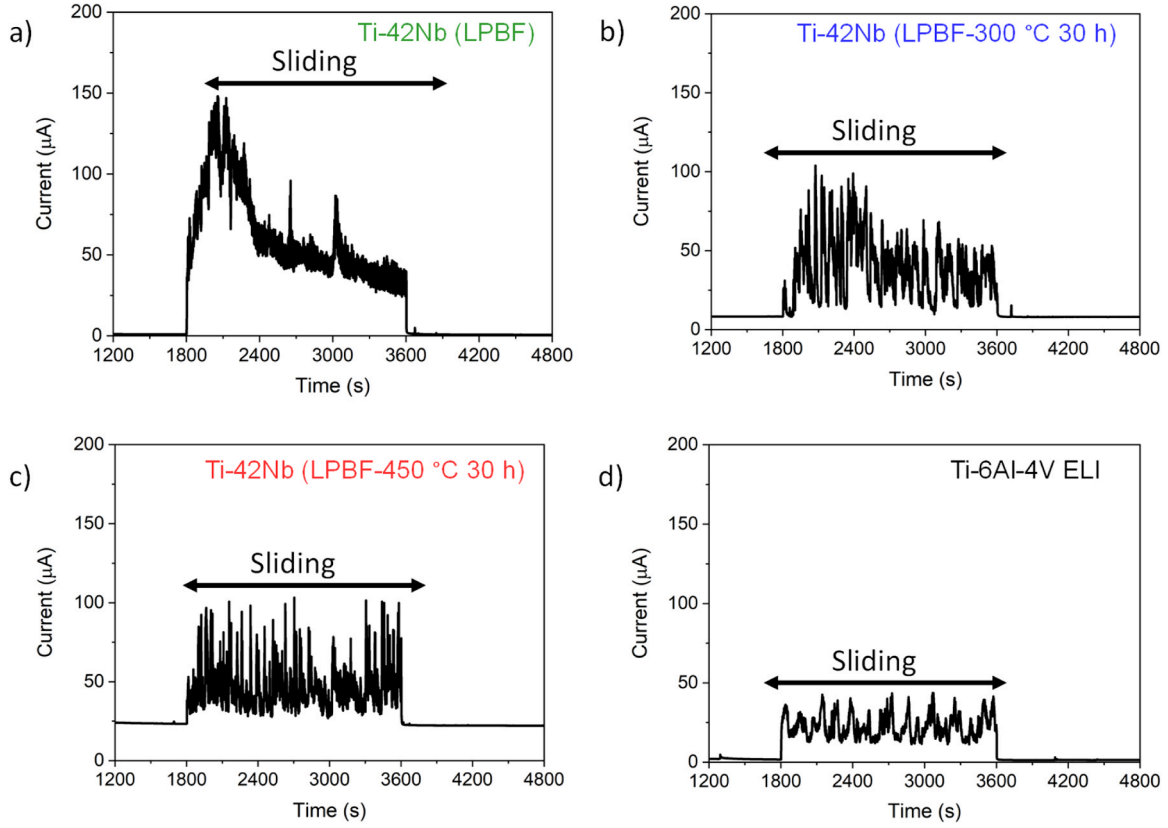

Fig. 6. Current evaluation for a) Ti-42Nb (LPBF), b) Ti-42Nb (LPBF-300°C 30 h), c) Ti-42Nb (LPBF-450°C 30 h), and d) Ti-6Al-4V ELI alloys under anodic potentiostatic polarization (0.6 V vs. Ag|AgCl) conditions in PBS. The arrows indicate the reciprocating sliding occurring between 1800 s and 3600 s.

Table 1
The determined electrochemical parameters for Ti-42Nb (LPBF), Ti-42Nb (LPBF-300 °C 30 h), Ti-42Nb (LPBF-450 °C 30 h), and Ti-6Al-4V ELI alloy states, extracted from the anodic potentiostatic polarization (0.6 V vs. Ag|AgCl) curves.

	Current before sliding $I_{initial}$ (μA)	Current during sliding I_{wear} (μA)	Current after sliding I_{final} (μA)
Ti−42Nb (LPBF)	1.7 ± 0.2	48.4 ± 19.3	1.6 ± 1.1
Ti−42Nb (LPBF−300 °C 30 h)	8.7 ± 1.7	33.5 ± 8.1	6.9 ± 1.6
Ti−42Nb (LPBF−450 °C 30 h)	26.6 ± 4.1	39.9 ± 8.7	25.6 ± 2.6
Ti−6Al-4V ELI	2.8 ± 1.5	27.4 ± 7.1	0.9 ± 0.7

surfaces under OCP conditions are shown in Fig. 7, and corresponding 3D optical profilometry results are illustrated in Fig. 8.

Worn surfaces after tribocorrosion tests (under OCP conditions) exhibit grooves (blue arrows), which are typical for Ti and its alloys [56–58]. During sliding, the formation of wear debris, as seen in Fig. 7 (orange arrows), is quite natural due to the repetitive transfer of the studied material between the sliding surfaces. As discussed previously in our work [44], the degradation mechanism involves a combination of abrasive and adhesive wear, resulting from the presence of grooves and wear debris within the wear track.

The grooves (blue arrows in Fig. 7) are much shallower with a superficial nature for the Ti-6Al-4V ELI alloy. The grooves are wider and deeper for age-hardened LPBF-produced Ti-42Nb alloys compared to LPBF-produced as-built alloy and Ti-6Al-4V ELI.

Among LPBF-produced specimens, the worn surface morphology is similar (deep grooves and severe wear debris accumulation). However, LPBF-produced as-built alloys exhibit a relatively smooth worn area compared to age-hardened alloys.

To quantify the tribological parameters, wear volume loss (V_{tot}), average wear depth (D), and worn area were calculated from the 3D confocal profilometry measurements (Fig. 8), as reported in Table 2. The results indicated that Ti-6Al-4V ELI exhibited less material loss (with the lowest wear volume loss, lowest average wear depth and worn area), while LPBF-produced age-hardened alloys exhibited more severe wear with the high wear volume loss and average depth under OCP conditions. However, LPBF-produced as-built alloys exhibited smaller wear volume losses and wear depth values than age-hardened alloys.

In addition, the evolution of the coefficient of friction (COF) during sliding under OCP conditions was also recorded with the help of a tribometer. The COF values for the

studied alloys are similar (0.42 and 0.48 LPBF-produced age-hardened alloys, 300 °C 30 h and 450 °C 30 h, respectively) and lower than the LPBF-produced as-built (0.64). In addition, Ti-6Al-4V ELI (0.43) exhibits quite similar COF values to LPBF-produced age-hardened alloys. However, COF values reflect the material's lubrication behaviour and are not directly linked to its wear performance [59,60].

For detailed analysis of the worn areas, two alloys (Ti-42Nb (LPBF-300 °C 30 h) and Ti-6Al-4V ELI) were selected from those tested under anodic potentiostatic polarization. These alloys exemplify two opposite ends of the spectrum in terms of volume loss during OCP sliding, enabling a comparison of overall material loss and wear characteristics. The wear depth and total volume loss under anodic potentiostatic polarization (0.6 V vs. Ag|AgCl) conditions for Ti-42Nb (LPBF-300 °C 30 h) and Ti-6Al-4V ELI alloys were evaluated using SEM and 3D optical profilometry, as illustrated in Fig. 9. SEM images (Fig. 9b and d) showed a similar degradation mechanism compared to the OCP conditions, with the combination of abrasive and adhesive wear. However, the worn surfaces have a less rough appearance compared to the ones under OCP conditions. This could be associated with anodic potentiostatic

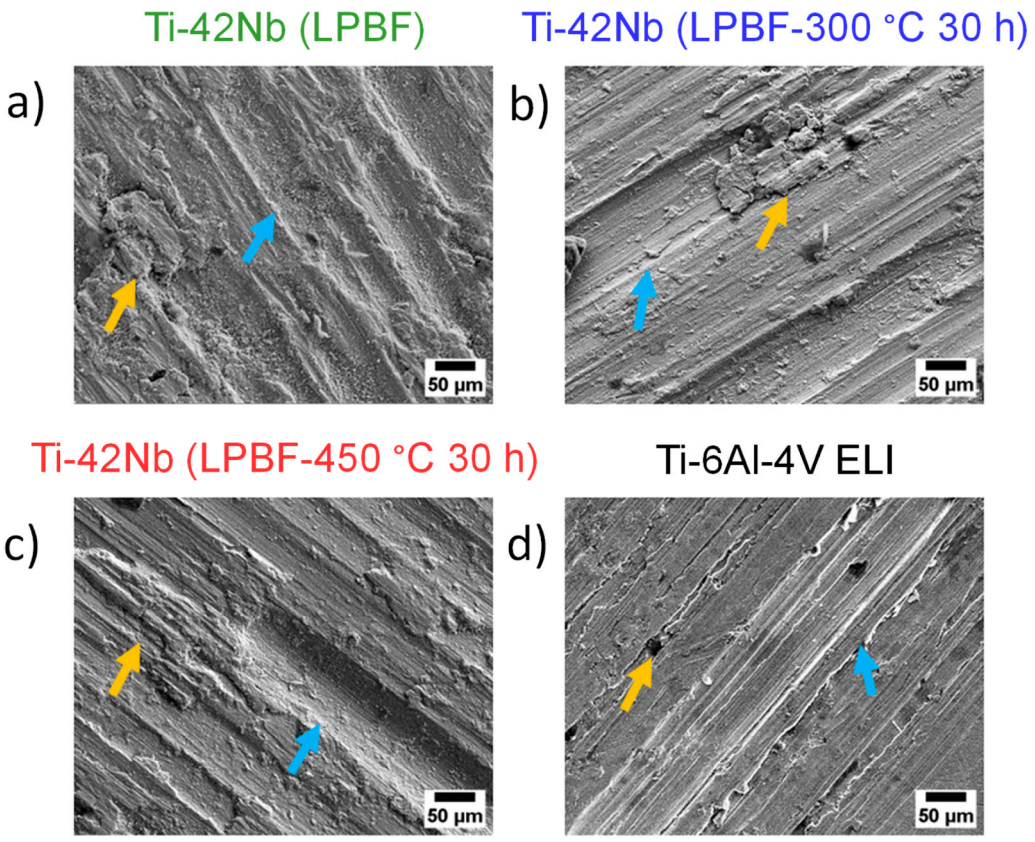

Fig. 7. Secondary electron (SE) images of the wear tracks formed under OCP conditions for a) Ti-42Nb (LPBF), b) Ti-42Nb (LPBF-300 °C 30 h), c) Ti-42Nb (LPBF-450 °C 30 h), and d) Ti-6Al-4V ELI alloy states. In wear tracks, orange arrows represent the wear debris, and blue ones represent the groove formation.

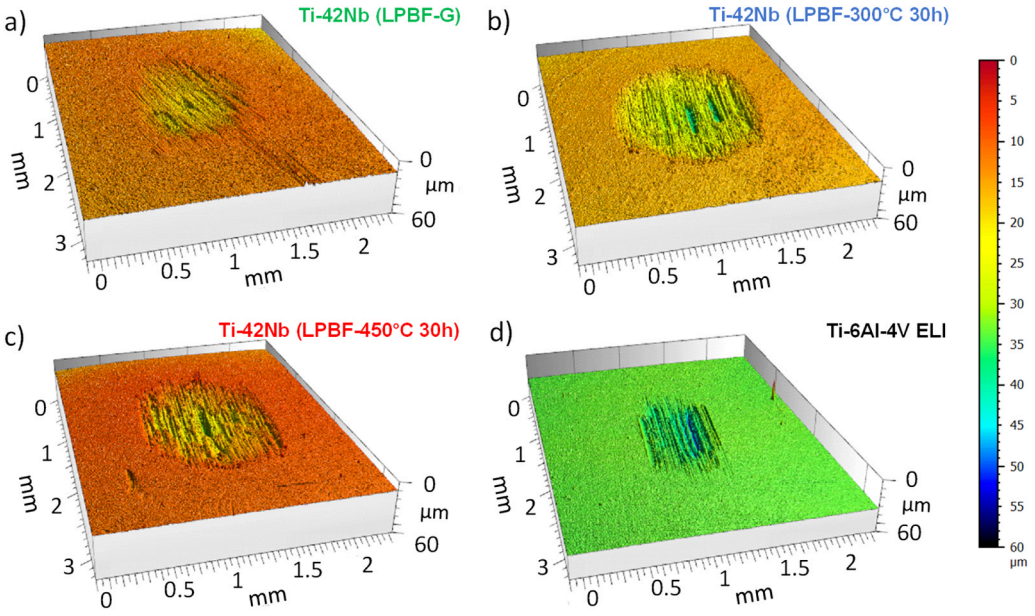

Fig. 8. 3D optical profilometry images of the wear tracks formed under OCP conditions for a) Ti-42Nb (LPBF), b) Ti-42Nb (LPBF-300 °C 30 h), c) Ti-42Nb (LPBF-450 °C 30 h), and d) Ti-6Al-4V ELI alloy states.

polarization since smoother material removal can be achieved through anodic polarization, which may lead to a more uniform dissolution process, preventing the formation of deep grooves and rough wear scars that typically occur under OCP conditions. The oxide layer, while not significantly reducing wear loss, can fill in micro-defects and act as a temporary smoothing agent during sliding contact, contributing to a smoother surface. The wear depth and volume loss were calculated as 6.81 ± 2.65 µm and $15.06 \pm 4.48 \times 10^{-3}$ mm^3 for Ti-42Nb (LPBF-300 °C 30 h), respectively, from the 3D optical profilometry measurements (Fig. 9a and c). For Ti-6Al-4V ELI, the wear depth and volume loss were calculated as 2.23 ± 0.56 µm and $2.92 \pm 0.80 \times 10^{-3}$ mm^3, respectively. The total volume loss during anodic polarization is similar for

Table 2
The average depth (D) of the wear tracks, together with the worn area and total volume loss (V_{tot}) under OCP conditions, was determined for the studied alloys from 3D optical profilometry measurements.

	Wear depth D (μm)	Worn area (mm²)	Total volume loss V_{tot} x 10^{-3} (mm³)
Ti−42Nb (LPBF)	3.89 ± 0.52	1.14 ± 0.04	4.41 ± 0.42
Ti−42Nb (LPBF−300 °C 30 h)	6.81 ± 0.53	2.13 ± 0.09	14.54 ± 1.84
Ti−42Nb (LPBF−450 °C 30 h)	5.36 ± 0.46	1.71 ± 0.05	9.16 ± 1.07
Ti−6Al-4V ELI	2.67 ± 0.24	0.98 ± 0.04	2.64 ± 0.36

both samples to that observed under OCP conditions (Table 2), indicating that the alloy samples undergo comparable wear mechanisms during reciprocating sliding motion in PBS.

4. Discussion

Laser powder bed fusion (LPBF) has gained attention for its flexibility in producing intricate geometries for patient-specific implants. LPBF-produced β-type Ti-Nb alloys offer superior mechanical properties and allow precise control over local properties by adjusting process parameters [34]. However, LPBF components often face mechanical anisotropy and residual stresses, necessitating post-heat treatment to refine microstructural and mechanical properties [37]. In this work, the novelty lies in its focus on post-heat-treated LPBF-produced β-type Ti-42Nb alloys, moving beyond prior studies that primarily investigated as-built Ti-42Nb [44]. This study uniquely integrates mechanical, corrosion, and tribocorrosion evaluations under realistic conditions, providing a comprehensive assessment relevant to biomedical applications. It highlights the role of controlled precipitate formation in influencing alloy performance and offers insights into the trade-offs between mechanical strengthening and tribocorrosion behaviour. By linking microstructural design with multi-property performance, this work provides practical guidance for optimizing Ti-42Nb alloys for implant use.

The application of isothermal heat treatment was found to be effective in increasing the mechanical properties of LPBF-produced bulk Ti-42Nb alloys by introducing ω_{iso} precipitates for Ti-42Nb (LPBF-300 °C 30 h) and α_{iso}'' precipitates for Ti-42Nb (LPBF-450 °C 30 h). The mechanical response of the alloy depends on the treatment conditions. In the as-built state, the alloy exhibits a yield strength of 700 ± 1 MPa, tensile strength of 715 ± 1 MPa, elongation of 20.1 ± 0.7 %, and a Young's modulus of 65 ± 1 GPa. Following heat treatment at 300 °C for 30 h, the yield strength rises to 850 ± 2 MPa and tensile strength to 835 ± 4 MPa, accompanied by a slight reduction in elongation to 17.9 ± 2.2 % and an increase in Young's modulus to 94 ± 5 GPa. Heat treatment at 450 °C for 30 h produces the highest strength values, with yield and tensile strengths of 1059 ± 17 MPa and 1124 ± 13 MPa, respectively, but significantly decreases elongation to 4.1 ± 0.5 % and yields a Young's modulus of 87 ± 1 GPa. Therefore, further research is essential to optimize the trade-off between achieving a low Young's modulus and enhancing mechanical strength, ensuring that both properties are effectively balanced to meet specific performance requirements for implant applications.

Regarding corrosion response, the studied alloys demonstrate similar and low corrosion current densities due to the formation of barrier-type passive films. In addition, the presence of ω_{iso} precipitates for Ti-42Nb (LPBF-300 °C 30 h) and the presence of α_{iso}'' precipitates for Ti-42Nb (LPBF-450 °C 30 h) do not yield a negative response in the passive film properties, indicating that stability is maintained. Even though the presence of precipitates contributes to corrosion and weakens the passive film during potentiodynamic polarization of Ti-Nb-based alloys [61, 62]. The overall corrosion response of the LPBF-produced β-type Ti-42Nb alloy is consistent, compared to conventionally produced Ti-6Al-4V ELI. This suggests that the chemical composition of the alloy, featuring two strongly passivating valve metals (Ti and Nb) in a

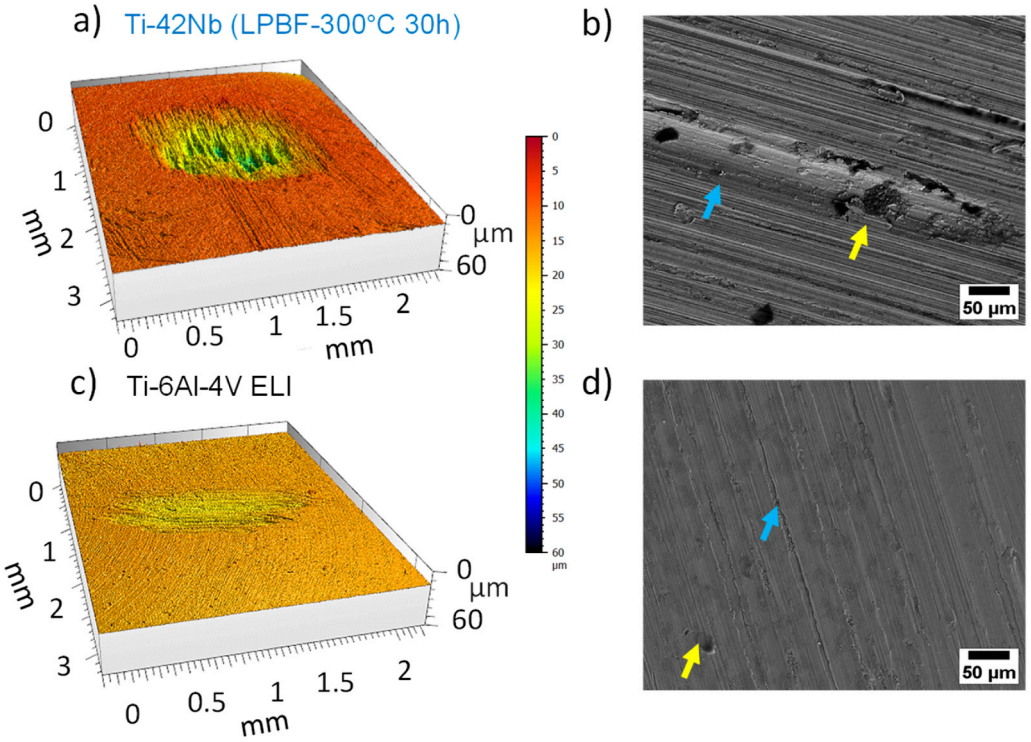

Fig. 9. 3D optical profilometry and secondary electron images of the wear tracks under anodic potentiostatic polarization conditions (0.6 V vs. Ag|AgCl) for a) and b) Ti-42Nb (LPBF-300 °C 30 h), as well as c) and d) Ti-6Al-4V ELI alloy states. In wear tracks, yellow arrows represent the wear debris, and blue ones represent the groove formation.

homogeneous solid solution, plays a more significant role than its microstructural features.

In tribocorrosion, the total volume loss arises from the combined effects of mechanical and chemical wear. Passive films that are highly reactive are more susceptible to depassivation when subjected to mechanical loads and require longer repassivation times compared to less reactive films. Delays in repassivation can exacerbate wear-accelerated corrosion, particularly under mechanical stress, further influencing the overall material degradation process [63]. However, in our case, mechanical wear plays a more dominant role under OCP conditions for the studied alloy samples due to the strong passivation nature of Ti alloys. Similar observations were made in studies of the tribocorrosion behaviour of Ti-Nb-Zr alloys in bovine serum against an alumina ball under OCP conditions [64]. Alberta et al. [43] also investigated the effect of Ga addition on the tribocorrosion performance of Ti-45Nb alloys in PBS against an alumina ball, reporting similar findings. However, in another study, Ti-Nb-Ta-O alloys were investigated in fetal bovine serum against a zirconia ball, and results show that tribocorrosion resistance was lowered with the presence of α precipitates compared to solution-treated states due to the formation of a thinner and non-uniform oxide layer with higher surface reactivity [62]. Thus, the findings reveal that special attention is needed to understand the effect of precipitates on the tribocorrosion behaviour of Ti alloys.

In this study, the post-treated LPBF-produced alloys demonstrated lower wear resistance under OCP conditions compared to both the LPBF-produced as-built alloys and the Ti-6Al-4V ELI alloy. The age-hardened alloys with high hardness (302 $HV_{0.1}$ and 335 $HV_{0.1}$, respectively, for Ti-42Nb (LPBF-300 °C 30 h) and Ti-42Nb (LPBF-450 °C 30 h)) exhibit higher total volume loss and wear depth. This discrepancy can be explained by the presence of hard and brittle precipitates in a soft matrix. The presence of ω_{iso} precipitates for Ti-42Nb (LPBF-300 °C 30 h) and the presence of α_{iso}'' precipitates for Ti-42Nb (LPBF-450 °C 30 h) alloys yield lower tribocorrosion response due to the possible detachment under reciprocating sliding, as illustrated schematically in Fig. 10.

Under sliding conditions, the quick detachment of hard and brittle precipitates from the softer matrix beta phase might generate higher volume losses due to the non-uniform hardness distribution along the material, as investigated before for aged lightweight steels [54], martensitic stainless steels [65], and cobalt-based alloys [66]. The tearing off of these precipitates intensifies the abrasive wear, acting as a third body [65]. Furthermore, the occurrence of high-intensity spikes during sliding under anodic polarization conditions may indicate the detachment of precipitates and the generation of higher volume loss for age-hardened alloys. Additionally, stacking faults can form at the boundary between the precipitate and matrix phases, leading to stress concentration, forming micro-cracks, and resulting in more significant wear loss [66]. Furthermore, the creation of micro-galvanic couples between the precipitate and boundary area speeds up alloy dissolution, leading to increased volume loss [66]. Thus, the size and distribution of the precipitates for the age-hardened LPBF-produced alloys need to be controlled carefully to combine proper mechanical properties with promising tribocorrosion performance for implant applications. The differences in total volume loss between age-hardened alloys follow Archard's law. Ti-42Nb (LPBF-450 °C 30 h) with higher hardness exhibits lower volume loss compared to the Ti-42Nb (LPBF-300 °C 30 h). Along with hardness and precipitate detachments, sub-surface strain deformation may also occur [67], influencing the tribocorrosion response and expanding the potential for further research.

The total volume loss during anodic potentiostatic polarization (0.6 V vs. Ag|AgCl) is anticipated to be greater than that observed under OCP conditions due to the combined influence of mechanical and chemical wear. This approach enables the evaluation of mechanisms beyond purely mechanical wear, such as wear-accelerated corrosion, and provides insights into the depassivation-repassivation kinetics of the surface. Although this potential is higher than typical physiological values, it offers a controlled condition to probe these processes. However, in age-hardened alloys, the total volume loss under anodic polarization is comparable to that recorded under OCP conditions. This resemblance may be linked to the formation of a discontinuous tribo-layer on the worn surface during sliding under anodic potentiostatic polarization. This tribo-layer could offer a protective effect against tribocorrosion by lowering current values during sliding, thereby serving as a barrier against material degradation or even functioning as a lubricant [55,68]. Consequently, the formation of the tribo-layer significantly limits the contribution of chemical wear. However, under mechanical loads, this layer may be removed by the pin during repetitive motions, leading to increased currents during sliding under anodic conditions [230]. Additionally, the detachment of hard and brittle precipitates can contribute to volume loss under anodic polarization, similar to what occurs under OCP conditions. Ultimately, the total volume loss under anodic polarization remains similar to that under OCP conditions, indicating that mechanical wear primarily influences the overall volume loss during anodic potentiostatic polarization.

5. Conclusions

This study examined the mechanical, corrosion, and tribocorrosion behaviour of LPBF-fabricated bulk Ti-42Nb alloys, in both as-built and post-heat-treated states, alongside conventionally manufactured Ti-6Al-4V ELI.

- Isothermal treatment was found to be effective in enhancing the mechanical properties of LPBF-produced Ti-42Nb alloys by introducing ω_{iso} precipitates for Ti-42Nb (LPBF-300 °C 30 h) and α_{iso}'' precipitates for Ti-42Nb (LPBF-450 °C 30 h). However, continued

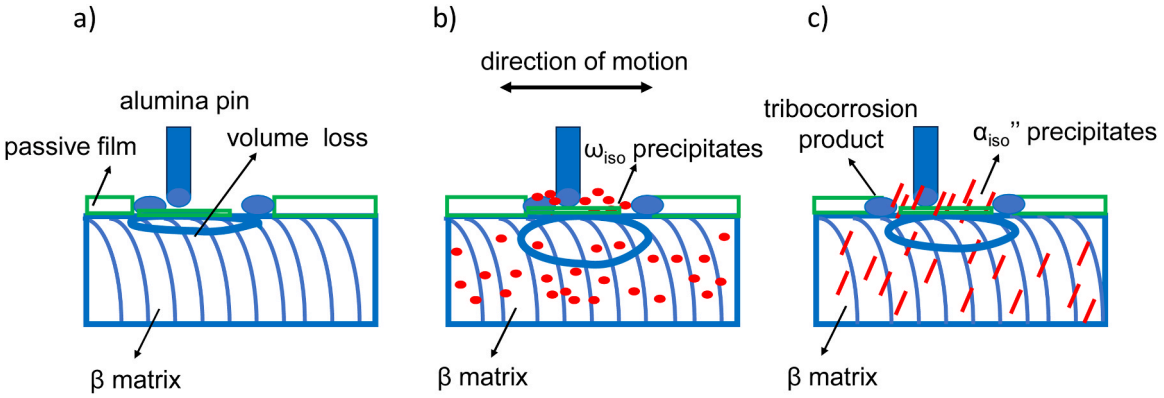

Fig. 10. Schematic representation of the tribocorrosion mechanism for LPBF-produced a) Ti-42Nb (LPBF), b) Ti-42Nb (LPBF-300 °C 30 h) and c) Ti-42Nb (LPBF-450 °C 30 h) alloys under reciprocating sliding against an alumina ball in PBS.

research is needed to better balance a low Young's modulus with improved mechanical strength.

- The LPBF-produced Ti-42Nb alloy variants exhibited similar overall corrosion performance in PBS, showing corrosion resistance comparable to that of Ti-6Al-4V ELI. This indicates that the passivating properties of Ti and Nb have a greater influence than differences in microstructure.
- Post-treated LPBF-produced alloys exhibit reduced wear resistance compared to as-built Ti-42Nb and Ti-6Al-4V ELI. Despite their higher hardness, these post-treated alloys experience greater total volume loss and deeper wear tracks. This behaviour may be related to the presence of hard and brittle precipitates, with the possible detachment of ω_{iso} precipitates in Ti-42Nb (LPBF-300 °C 30 h) and α_{iso}'' precipitates in Ti-42Nb (LPBF-450 °C 30 h), potentially contributing to reduced tribocorrosion performance.

In summary, the LPBF-produced bulk Ti-42Nb alloy in the as-built state exhibits promising tribocorrosion behaviour, though it still falls short compared to the performance of conventional Ti-6Al-4V ELI. Post-heat-treated Ti-42Nb alloys demonstrate even less robust tribocorrosion resistance than the as-built state (non-heat-treated). Nonetheless, tailoring the distribution of precipitates may offer a pathway to improve their tribocorrosion properties, but comprehensive subsurface investigations are crucial to reveal deformation layers, subsurface cracks, precipitate-matrix interactions, and other microstructural features that govern tribocorrosion mechanisms. Such studies are essential to fully understand how post-heat treatments modify the microstructure and influence critical implant-relevant properties, including corrosion and tribocorrosion, and to guide the optimization of LPBF-produced Ti-42Nb alloys for biomedical applications.

CRediT authorship contribution statement

Martina Zimmermann: Writing – review & editing, Supervision, Resources, Project administration, Funding acquisition, Conceptualization. **Annett Gebert:** Writing – review & editing, Validation, Supervision, Resources, Project administration, Methodology, Funding acquisition. **Stefan Pilz:** Visualization, Investigation. **Nicolas Courtois:** Writing – review & editing, Validation, Supervision, Funding acquisition. **Benoit Ter-Ovanessian:** Writing – review & editing, Methodology. **Christian Haase:** Writing – review & editing, Validation, Supervision. **Ana-Maria Trunfio Sfarghiu:** Supervision, Methodology. **Jaqueline Gehlmann:** Writing – review & editing, Investigation. **Avinash Hariharan:** Writing – review & editing, Visualization, Investigation, Formal analysis. **Adnan Akman:** Writing – review & editing, Writing – original draft, Visualization, Validation, Methodology, Investigation, Formal analysis, Data curation, Conceptualization. **Yohan Douest:** Software, Investigation, Formal analysis.

Funding information

A.A. and Y.D. are grateful for the financial support from the European Commission within the H2020-MSCA grant agreement No. 861046 (BIOREMIA-ETN). A.G. and M.Z. acknowledge funding by the Deutsche Forschungsgemeinschaft (DFG) under projects GE/1106/12–2 and ZI/1006/16–2 no 419952351. We acknowledge DESY (Hamburg, Germany), a member of the Helmholtz Association HGF, for the provision of experimental facilities. Parts of this research were carried out at PETRA III, and we would like to thank Emad Maawad for assistance in using beamline P07. Beamtime was allocated for proposal I-20220421.

Declaration of Competing Interest

The authors declare that they have no known competing financial interests or personal relationships that could have appeared to influence the work reported in this paper.

Acknowledgements

The authors are grateful to Bernard Normand (INSA Lyon) and Nicolas Mary (INSA Lyon) for fruitful scientific discussions. Yosra Chrigui (INSA Lyon) is acknowledged for assistance during tribocorrosion experiments.

Data Availability

Data will be made available on request.

References

[1] M. Geetha, A.K. Singh, R. Asokamani, A.K. Gogia, Ti based biomaterials, the ultimate choice for orthopaedic implants - A review, Prog. Mater. Sci. 54 (3) (2009) 397–425, https://doi.org/10.1016/j.pmatsci.2008.06.004.

[2] K. Miura, N. Yamada, S. Hanada, T.K. Jung, E. Itoi, The bone tissue compatibility of a new Ti-Nb-Sn alloy with a low Young's modulus, Acta Biomater. 7 (5) (2011) 2320–2326, https://doi.org/10.1016/j.actbio.2011.02.008.

[3] L.C. Zhang, H. Attar, M. Calin, J. Eckert, Review on manufacture by selective laser melting and properties of titanium based materials for biomedical applications, Mater. Technol. 31 (2) (2016) 66–76, https://doi.org/10.1179/1753555715Y.0000000076.

[4] J.V. Calazans Neto, C.A.S. Celles, C.S.A.F. de Andrade, C.R.M. Afonso, B.E. Nagay, V.A.R. Barão, Recent advances and prospects in β-type titanium alloys for dental implants applications, ACS Biomater. Sci. Eng. (2024), https://doi.org/10.1021/acsbiomaterials.4c00963.

[5] L.A. Alberta, J. Vishnu, A. Hariharan, S. Pilz, A. Gebert, M. Calin, Novel low modulus beta-type Ti-Nb alloys by gallium and copper minor additions for antibacterial implant applications, J. Mater. Res. Technol. 20 (2022) 3306–3322, https://doi.org/10.1016/j.jmrt.2022.08.111.

[6] A. Helth, et al., Effect of thermomechanical processing on the mechanical biofunctionality of a low modulus Ti-40Nb alloy, J. Mech. Behav. Biomed. Mater. 65 (2017) 137–150, https://doi.org/10.1016/j.jmbbm.2016.08.017.

[7] S. Pilz, et al., Metal release and cell biological compatibility of beta-type Ti-40Nb containing indium, J. Biomed. Mater. Res. Part B Appl. Biomater. 106 (5) (2018) 1686–1697, https://doi.org/10.1002/jbm.b.33976.

[8] A. Helth, et al., Chemical nanoroughening of Ti40Nb surfaces and its effect on human mesenchymal stromal cell response, J. Biomed. Mater. Res. Part B Appl. Biomater. 102 (1) (2014) 31–41, https://doi.org/10.1002/jbm.b.32976.

[9] A. Hariharan, et al., Single- and multiscale laser patterning of 3D printed biomedical titanium alloy: toward an enhanced adhesion and early differentiation of human bone marrow stromal cells, Adv. Funct. Mater. 34 (8) (2024) 1–16, https://doi.org/10.1002/adfm.202310607.

[10] A. Akman, et al., Effect of minor gallium addition on corrosion, passivity, and antibacterial behaviour of novel β-type Ti-Nb alloys, J. Mater. Res. Technol. 25 (2023) 4110–4124, https://doi.org/10.1016/j.jmrt.2023.06.219.

[11] A. Gebert, et al., Effect of indium (In) on corrosion and passivity of a beta-type Ti-Nb alloy in Ringer's solution, Appl. Surf. Sci. 335 (2015) 213–222, https://doi.org/10.1016/j.apsusc.2015.02.058.

[12] P.F. Gostin, et al., Surface treatment, corrosion behavior, and apatite-forming ability of ti-45Nb implant alloy (B), J. Biomed. Mater. Res. Part B Appl. Biomater. Vol. 101 (2) (2013) 269–278, https://doi.org/10.1002/jbm.b.32836.

[13] M. Niinomi, Y. Liu, M. Nakai, H. Liu, H. Li, Biomedical titanium alloys with Young's moduli close to that of cortical bone, Regen. Biomater. 3 (3) (2016) 173–185, https://doi.org/10.1093/RB/RBW016.

[14] S. Pilz, et al., Thermomechanical processing of In-containing β-type Ti-Nb alloys, no. December 2017, J. Mech. Behav. Biomed. Mater. 79 (2018) 283–291, https://doi.org/10.1016/j.jmbbm.2017.12.028.

[15] M. Nakai, M. Niinomi, T. Oneda, Improvement in fatigue strength of biomedical β-type Ti-Nb-Ta-Zr alloy while maintaining low young's modulus through optimizing ω-phase precipitation, Metall. Mater. Trans. A Phys. Metall. Mater. Sci. 43 (1) (2012) 294–302, https://doi.org/10.1007/s11661-011-0860-3.

[16] M. Qiang et al., "Enhanced strength and reduced elastic modulus of biomedical metastable β Ti–Nb alloy via intermediate phase transformation," Mater. Des., vol. 251, no. September 2024, p. 113662, 2025, doi: 10.1016/j.matdes.2025.113662.

[17] T. Akahori, M. Niinomi, H. Fukui, A. Suzuki, Fatigue, fretting fatigue and corrosion characteristics of biocompatible beta type titanium alloy conducted with various thermo-mechanical treatments, Mater. Trans. 45 (5) (2004) 1540–1548, https://doi.org/10.2320/matertrans.45.1540.

[18] T. Akahori, M. Niinomi, H. Fukui, M. Ogawa, H. Toda, Improvement in fatigue characteristics of newly developed beta type titanium alloy for biomedical applications by thermo-mechanical treatments, Mater. Sci. Eng. C. 25 (3) (2005) 248–254, https://doi.org/10.1016/j.msec.2004.12.007.

[19] M.J. Lai, T. Li, F.K. Yan, J.S. Li, D. Raabe, Revisiting ω phase embrittlement in metastable β titanium alloys: Role of elemental partitioning, Scr. Mater. 193 (2021) 38–42, https://doi.org/10.1016/j.scriptamat.2020.10.031.

[20] H. Matsumoto, S. Watanabe, S. Hanada, Microstructures and mechanical properties of metastable β TiNbSn alloys cold rolled and heat treated, J. Alloy. Compd. 439 (1–2) (2007) 146–155, https://doi.org/10.1016/j.jallcom.2006.08.267.

[21] J. Coakley, K.M. Rahman, V.A. Vorontsov, M. Ohnuma, D. Dye, Effect of precipitation on mechanical properties in the β-Ti alloy Ti-24Nb-4Zr-8Sn, Mater. Sci. Eng. A 655 (2016) 399–407, https://doi.org/10.1016/j.msea.2015.12.024.

[22] M. Bönisch, et al., Thermal stability and phase transformations of martensitic Ti-Nb alloys, Sci. Technol. Adv. Mater. 14 (5) (2013), https://doi.org/10.1088/1468-6996/14/5/055004.

[23] J. Sun, Q. Yao, H. Xing, W.Y. Guo, Elastic properties of β, α″ and ω metastable phases in Ti-Nb alloy from first-principles, J. Phys. Condens. Matter 19 (48) (2007), https://doi.org/10.1088/0953-8984/19/48/486215.

[24] S. Pilz, A. Hariharan, F. Günther, M. Zimmermann, A. Gebert, Influence of isothermal omega precipitation aging on deformation mechanisms and mechanical properties of a β-type Ti-Nb alloy, J. Alloy. Compd. 930 (2023) 167309, https://doi.org/10.1016/j.jallcom.2022.167309.

[25] S. Pilz, et al., Tailoring microstructure and mechanical properties of an LPBF-processed beta Ti-Nb alloy through post-heat treatments (no. February), Mater. Des. 239 (2024), https://doi.org/10.1016/j.matdes.2024.112799.

[26] T. Majumdar, N. Eisenstein, J.E. Frith, S.C. Cox, N. Birbilis, Additive Manufacturing of Titanium Alloys for Orthopedic Applications: A Materials Science Viewpoint, Adv. Eng. Mater. 20 (9) (2018), https://doi.org/10.1002/adem.201800172.

[27] E. Alabort, Y.T. Tang, D. Barba, R.C. Reed, Alloys-by-design: a low-modulus titanium alloy for additively manufactured biomedical implants, Acta Mater. 229 (2022), https://doi.org/10.1016/j.actamat.2022.117749.

[28] A. Hariharan, et al., Designing the microstructural constituents of an additively manufactured near β Ti alloy for an enhanced mechanical and corrosion response, Mater. Des. 217 (2022) 110618, https://doi.org/10.1016/j.matdes.2022.110618.

[29] F. Günther, et al., Defect-dependent fatigue properties of β Ti-42Nb processed by laser powder bed fusion, no. December 2024, Mater. Today Commun. 43 (2025), https://doi.org/10.1016/j.mtcomm.2025.111733.

[30] F. Günther, et al., Characterization of additively manufactured lumbar interbody fusion cages based on triply periodic minimal surfaces (no. January), Mater. Today Commun. 39 (2024) 108634, https://doi.org/10.1016/j.mtcomm.2024.108634.

[31] F. Günther, et al., Experimental and numerical characterization of imperfect additively manufactured lattices based on triply periodic minimal surfaces, no. June 233 (2023).

[32] F. Günther, M. Wagner, S. Pilz, A. Gebert, M. Zimmermann, Design procedure for triply periodic minimal surface based biomimetic scaffolds, no. October 2021, J. Mech. Behav. Biomed. Mater. 126 (2022) 104871, https://doi.org/10.1016/j.jmbbm.2021.104871.

[33] F. Günther, et al., Structure-property relationships of imperfect additively manufactured lattices based on triply periodic minimal surfaces, Mater. Des. 222 (2022), https://doi.org/10.1016/j.matdes.2022.111036.

[34] S. Pilz, T. Gustmann, F. Günther, M. Zimmermann, U. Kühn, A. Gebert, Controlling the Young's modulus of a ß-type Ti-Nb alloy via strong texturing by LPBF, Mater. Des. 216 (2022) 110516, https://doi.org/10.1016/j.matdes.2022.110516.

[35] J.J. Marattukalam, et al., The effect of laser scanning strategies on texture, mechanical properties, and site-specific grain orientation in selective laser melted 316L SS, Mater. Des. 193 (2020), https://doi.org/10.1016/j.matdes.2020.108852.

[36] T. Nagase, T. Hori, M. Todai, S.H. Sun, T. Nakano, Additive manufacturing of dense components in beta-titanium alloys with crystallographic texture from a mixture of pure metallic element powders, Mater. Des. 173 (2019) 107771, https://doi.org/10.1016/j.matdes.2019.107771.

[37] M. Laleh, et al., Heat treatment for metal additive manufacturing, no. November 2022, Prog. Mater. Sci. 133 (2023) 101051, https://doi.org/10.1016/j.pmatsci.2022.101051.

[38] M. Hein, et al., Heat treatments of metastable β titanium alloy Ti-24Nb-4Zr-8Sn processed by laser powder bed fusion, Mater. (Basel) 15 (11) (2022), https://doi.org/10.3390/ma15113774.

[39] C.E.P. Talbot, N.L. Church, E.M. Hildyard, L.D. Connor, J.R. Miller, N.G. Jones, On the stability and formation of the α″ and ω phases in Ti-Nb alloys upon cooling, no. May 2023, Acta Mater. 262 (2024) 119409, https://doi.org/10.1016/j.actamat.2023.119409.

[40] D. Landolt, S. Mischler, M. Stemp, Electrochemical methods in tribocorrosion: a critical appraisal, Electrochim. Acta 46 (24–25) (2001) 3913–3929, https://doi.org/10.1016/S0013-4686(01)00679-X.

[41] S. Mischler, Triboelectrochemical techniques and interpretation methods in tribocorrosion: a comparative evaluation, Tribol. Int. 41 (7) (2008) 573–583, https://doi.org/10.1016/j.triboint.2007.11.003.

[42] A. Revathi, S. Magesh, V.K. Balla, M. Das, G. Manivasagam, "Current advances in enhancement of wear and corrosion resistance of titanium alloys – a review,", Mater. Technol. 31 (12) (2016) 696–704, https://doi.org/10.1080/10667857.2016.1212780.

[43] L. Andrea, et al., Tribology international tribocorrosion behavior of β -type Ti-Nb-Ga alloys in a physiological solution (no. January), Tribol. Int. 181 (2023) 108325, https://doi.org/10.1016/j.triboint.2023.108325.

[44] A. Akman, et al., Tribocorrosion behaviour of additively manufactured β-type Ti–Nb alloy for implant applications (no. June), J. Mater. Res. Technol. 31 (2024) 1419–1429, https://doi.org/10.1016/j.jmrt.2024.06.172.

[45] P. Goldberg, et al., Fine-tuning effect of Direct Laser Interference Patterning on the surface states and the corrosion behavior of a biomedical additively manufactured beta Ti alloy (no. January), Corros. Sci. 219 (2023), https://doi.org/10.1016/j.corsci.2023.111230.

[46] P. Barriobero-Vila, G. Requena, S. Schwarz, F. Warchomicka, T. Buslaps, Influence of phase transformation kinetics on the formation of α in a β-quenched Ti-5Al-5Mo-5V-3Cr-1Zr alloy, Acta Mater. 95 (2015) 90–101, https://doi.org/10.1016/j.actamat.2015.05.008.

[47] A. Dehghan-Manshadi, R.J. Dippenaar, Development of α-phase morphologies during low temperature isothermal heat treatment of a Ti-5Al-5Mo-5V-3Cr alloy, Mater. Sci. Eng. A 528 (3) (2011) 1833–1839, https://doi.org/10.1016/j.msea.2010.09.061.

[48] D.L. Gong, et al., Temperature-independent resistivity in a Ti-Nb-based titanium alloy with a compositionally-modulated dual-phase microstructure, J. Alloy. Compd. 955 (2023), https://doi.org/10.1016/j.jallcom.2023.170267.

[49] D. Gong, et al., Tuning temperature coefficient of elastic modulus by heat treatment in a compositionally-modulated Ti-Nb-based alloy, no. December 2022, Scr. Mater. 227 (2023) 115275, https://doi.org/10.1016/j.scriptamat.2022.115275.

[50] A. Reck, et al., Effects of thermomechanical history and environment on the fatigue behavior of (β)-Ti-Nb implant alloys, MATEC Web Conf. 165 (2018) 1–8, https://doi.org/10.1051/matecconf/201816506001.

[51] Y. Bai, et al., Characterization, corrosion behavior, cellular response and in vivo bone tissue compatibility of titanium-niobium alloy with low Young's modulus, Mater. Sci. Eng. C. 59 (2016) 565–576, https://doi.org/10.1016/j.msec.2015.10.062.

[52] H.Y. Kim, Y. Ikehara, J.I. Kim, H. Hosoda, S. Miyazaki, Martensitic transformation, shape memory effect and superelasticity of Ti-Nb binary alloys, Acta Mater. 54 (9) (2006) 2419–2429, https://doi.org/10.1016/j.actamat.2006.01.019.

[53] M.J. Lai, T. Li, D. Raabe, Ω Phase acts as a switch between dislocation channeling and joint twinning- and transformation-induced plasticity in a metastable B titanium alloy, Acta Mater. 151 (2018) 67–77, https://doi.org/10.1016/j.actamat.2018.03.053.

[54] Y. Tang, et al., Tribology, corrosion, and tribocorrosion performance of aged lightweight steels: effects of oxide film and carbide (no. March), Corros. Sci. 231 (2024), https://doi.org/10.1016/j.corsci.2024.111999.

[55] I. Çaha, et al., Interactions between wear and corrosion on cast and sintered Ti-12Nb alloy in comparison with the commercial Ti-6Al-4V alloy (no. August), Corros. Sci. 176 (2020) 108925, https://doi.org/10.1016/j.corsci.2020.108925.

[56] I. Çaha, et al., Degradation behavior of Ti-Nb alloys: corrosion behavior through 21 days of immersion and tribocorrosion behavior against alumina, Corros. Sci. 167 (2020) 108488, https://doi.org/10.1016/j.corsci.2020.108488.

[57] J. Ureña, S. Tsipas, A.M. Pinto, F. Toptan, E. Gordo, A. Jiménez-Morales, Corrosion and tribocorrosion behaviour of β-type Ti-Nb and Ti-Mo surfaces designed by diffusion treatments for biomedical applications (no. June), Corros. Sci. 140 (2018) 51–60, https://doi.org/10.1016/j.corsci.2018.06.024.

[58] F. Toptan, et al., Corrosion and tribocorrosion behaviour of Ti6Al4V produced by selective laser melting and hot pressing in comparison with the commercial alloy, J. Mater. Process. Technol. 266 (2019) 239–245, https://doi.org/10.1016/j.jmatprotec.2018.11.008.

[59] N. Hua, W. Chen, Q. Wang, Q. Guo, Y. Huang, T. Zhang, Tribocorrosion behaviors of a biodegradable Mg65Zn30Ca5 bulk metallic glass for potential biomedical implant applications, J. Alloy. Compd. 745 (2018) 111–120, https://doi.org/10.1016/j.jallcom.2018.02.138.

[60] A.I. Muñoz, A. Dalmau, S. Mischler, Alumina/metal tribopairs: which is the wearing element under tribocorrosion conditions?, no. December 2024, Wear (2025) 205816, https://doi.org/10.1016/j.wear.2025.205816.

[61] Q. Li, J. Li, G. Ma, X. Liu, D. Pan, Influence of ω phase precipitation on mechanical performance and corrosion resistance of Ti–Nb–Zr alloy, Mater. Des. 111 (2016) 421–428, https://doi.org/10.1016/j.matdes.2016.09.026.

[62] S. Acharya, et al., Role of aging induced α precipitation on the mechanical and tribocorrosive performance of a β Ti-Nb-Ta-O orthopedic alloy (no. May), Mater. Sci. Eng. C. 103 (2019) 109755, https://doi.org/10.1016/j.msec.2019.109755.

[63] S. Mischler, A. Spiegel, M. Stemp, D. Landolt, Influence of passivity on the tribocorrosion of carbon steel in aqueous solutions, Wear 251 (2001) 1295–1307.

[64] M.Q. Neto, W.M. Rainforth, Effect of potential and microstructure on the tribocorrosion behaviour of beta and near beta Ti Alloys II, J. Bio TriboCorros. 7 (4) (2021) 1–12, https://doi.org/10.1007/s40735-021-00578-5.

[65] Y. Zhou, Z. Zhao, S. Jiang, D. Duan, Effect of heat treatment on the tribocorrosion behavior of 20Cr13 martensitic stainless steel (no. March), Tribol. Int. 197 (2024), https://doi.org/10.1016/j.triboint.2024.109768.

[66] Z. Wang, Y. Yan, L. Xing, Y. Su, L. Qiao, The role of hard phase carbides in tribocorrosion processes for a Co-based biomedical alloy, no. July 2016, Tribol. Int. 113 (2017) 370–376, https://doi.org/10.1016/j.triboint.2017.01.037.

[67] M. Long, H.J. Rack, Subsurface deformation and microcrack formation in Ti-35Nb-8Zr-5Ta-O(x) during reciprocating sliding wear, Mater. Sci. Eng. C. 25 (3) (2005) 382–388, https://doi.org/10.1016/j.msec.2005.01.027.

[68] I. Çaha, et al., Corrosion and tribocorrosion behavior of Ti-40Nb and Ti-25Nb-5Fe alloys processed by powder metallurgy, Metall. Mater. Trans. A Phys. Metall. Mater. Sci. 51 (6) (2020) 3256–3267, https://doi.org/10.1007/s11661-020-05757-6.